Article

Not peer-reviewed version

# Multiscale Multiphysics Modeling of Aqueous Humor Dynamics in the Human Eye

Riccardo Sacco *, Greta Chiaravalli, Giovanna Guidoboni, Anita Layton, Gal Antman, Keren Wood Shalem, Alice Verticchio, Brent Siesky, Thomas A.Ciulla, Alon Harris

Posted Date: 3 June 2026

doi: 10.20944/preprints202606.0250.v1

Keywords: multiscale multiphysics modeling; simulation; ophthalmology; aqueous humor; compartment models; solute and ion transport; semipermeable membranes

 doi:10.20944/preprints202606.0250.v1



*Article*

# Multiscale Multiphysics Modeling of Aqueous Humor Dynamics in the Human Eye

**Riccardo Sacco [1,*], Greta Chiaravalli [2], Giovanna Guidoboni [3], Anita Layton [4], Gal Antman [5,6], Keren Wood Shalem [7], Alice Verticchio [7], Brent Siesky [7], Thomas A. Ciulla [8] and Alon Harris [7]**

[1] Dipartimento di Matematica, Politecnico di Milano, Piazza Leonardo da Vinci 32 20133, Milano Italy
[2] Dipartimento di Fisica, Politecnico di Milano, Piazza Leonardo da Vinci 32 20133, Milano Italy
[3] Maine College of Engineering and Computing, University of Maine, 200 AMC Building, Orono, ME 04469, USA
[4] Department of Applied Mathematics, University of Waterloo, 200 University Ave W, Waterloo, ON N2L 3G1, Canada
[5] Department of Ophthalmology, Rabin Medical Center, Zeev Jabotinsky St 39, 4941492 Petah Tikva, Israel
[6] Faculty of Medicine, Tel Aviv University, Klachkin 35 Street, Tel Aviv, Israel
[7] Department of Ophthalmology, Icahn School of Medicine at Mount Sinai, 1468 Madison Avenue, Annenberg 22-86 New York, NY 10029, USA
[8] Indiana University School of Medicine, 340 West 10th Street, Indianapolis, IN 46202-3082, USA
* Correspondence: riccardo.sacco@polimi.it

**Abstract**

Aqueous humor (AH) is a watery fluid continuously circulating through the posterior and anterior chambers of the human eye and is essential to maintain a healthy intraocular pressure in the eye ball and keep the eye clean from waste products of metabolism and external agents. This paper presents a stationary compartment model of AH dynamics consisting of three integrated modules (M): M1 for AH production, M2 for AH passive flow and M3 for AH drainage. M1 is a zero-dimensional (0D) reduction of the velocity-extended Poisson-Nernst-Planck model and simulates solute transfer and fluid movement across the cellular structure of the ciliary epithelium (CE). M2 is the electric equivalent representation of Poiseuille flow across the series of two linear hydraulic resistors. M3 is a 0D reduction of the Darcy equations for a porous medium and simulates AH flow across the parallel between a nonlinear and a linear resistor. Compared to existing compartment approaches, the present model integrates at the macroscopic scale the multi-physical description of the human eye at the cellular scale. Numerical simulations suggest that (1) sodium channels in the CE are essential for maintaining proper AH dynamics; and (2) increased episcleral vein pressure reduces AH drainage, potentially explaining the development of secondary open-angle glaucoma. These insights advance the understanding of the mechanisms regulating AH dynamics and offer new perspectives for patient-specific therapies.

**Keywords:** multiscale multiphysics modeling; simulation; ophthalmology; aqueous humor; compartment models; solute and ion transport; semipermeable membranes

## 1. Introduction

The healthy turnover in production, flow and drainage of aqueous humor (AH) in the human eye is vital to ocular homeostasis and vision preservation. AH is a watery fluid continuously produced by the ciliary processes and slowly moving across the posterior and anterior chamber to be eventually drained out for successive recirculation. Experimental data indicate that in normal conditions the time to complete an entire recirculation cycle is about 90 minutes [1]. This allows us to mathematically assume AH dynamics to be a stationary process and safely neglect the dependence on the time variable. Homeostatic conditions (usually referred to as "baseline conditions") correspond to the situation where the volumetric flow rates (VFR) of produced, circulating and drained AH are equal to each other. In such conditions, measured data reported in [1] indicate that the baseline values of the AH VFR circulating in the eye and pressure in the eye (referred to as intraocular pressure, IOP) are $Q_{\mathrm{AH,b}} = 2.75\mu\mathrm{Lmin}^{-1}$ and $p_{\mathrm{IO,b}} = 15\mathrm{mmHg}$, respectively.

 doi:10.20944/preprints202606.0250.v1



The above described healthy situation undergoes a change under pathological conditions where IOP may depart from a range associated with "normal conditions". A significant example is primary open angle glaucoma (POAG), a disease of the optic nerve representing the second leading cause of blindness worldwide [2], for which the range is usually between 10 and 21 mmHg (see [3]). Another example is thyroid eye disease (TED), an autoimmune ocular pathology characterized by swelling and bulging of the eye globe due to inflammation and remodeling of the extraocular muscles [4], for which the baseline range for IOP is between 23 and 27 mmHg (see [5]). POAG and TED are multifactorial diseases whose causes have a different nature and act at very different spatial scales thereby making them unfavorable to disentanglement and often even unaccessible to measurement. For these reasons, availing of a mechanism-driven mathematical model, possibly integrated with artificial intelligence-based (AI) data-driven approaches, may result useful to shed light on the complex etiology of the considered disease (see [6,7]).

Mechanism-driven models can be classified into two main categories: compartment models (referred to as 0D models) and continuum models (referred to as $d$D models, $d = 1, 2, 3$). The construction of a 0D model usually leverages the analogy between fluid and electric variables (see [8, Chapter 15]) in which compartments are the nodes of an equivalent electric circuit and nodes are connected between each other by a resistor and to ground by a voltage or current source (see [9–12]). 0D models are computationally efficient but have the intrinsic limitation of neglecting the spatial variation of problem unknowns. This limitation is removed by the adoption of $d$D models which are constituted by systems of differential equations describing the multiphysical dynamics of AH, including fluid, mechanical and electrochemical phenomena (see [13–16]). $d$D models are characterized by a significant information content but have the limitation of requiring large computational resources to effectively deal with the wide multiscale nature of AH dynamics.

The objective of this study was to develop a mathematical and numerical model of AH dynamics capable of describing the physiology of the problem at each spatial scale while keeping the cost of the simulation at an affordable level. To this purpose, we introduced a stationary representation by compartments consisting of three integrated modules (M): M1 for AH production, M2 for AH passive flow and M3 for AH drainage. M1 takes into account the cellular composition of the production compartment, M2 and M3 the hydrodynamic characteristics and porous structure of passive flow and drainage compartments, respectively. M1 is the result of a 0D reduction of the velocity-extended Poisson-Nernst-Planck model (see [8, Chapter 13]) and simulates the transfer of neutral and charged solutes and fluid movement across the cellular structure of the ciliary epithelium (CE). M2 is the electric equivalent representation of Poiseuille flow across the series of two linear hydraulic resistors (see [13] and [8, Chapter 10]). M3 is a 0D reduction of the Darcy equations for a porous medium (see [17]) and simulates AH flow across a parallel connection of a nonlinear and linear resistors.

The proposed model was numerically implemented to comprehend how the findings of each module may help to explain the onset and progression of an ocular disease and to evaluate their impact on patient's health by contributing to develop specifically targeted therapeutical approaches. In particular, we used the integration of M1, M2 and M3 to give an answer to open questions about the role of (1) sodium channels in AH production and (2) episcleral vein pressure in AH drainage. Model predictions suggest that (1) the expression of sodium channels in the CE is essential for AH to flow from the ciliary processes into the posterior chamber; and (2) an increase of the episcleral vein pressure reduces AH drainage, potentially explaining the development of secondary open-angle glaucoma.

The structure of the paper is as follows. Section 2 illustrates the basic elements of the physiology of AH dynamics. Section 3 introduces the mathematical model of a biological semipermeable membrane. Section 4 illustrates the electric equivalent scheme of AH dynamics and its three-module composition. The multiscale equations of the model are described in Section 5 while the cellular mechanisms taking place in the CE are described in Section 6. Section 7 contains a description of the solution map that is adopted to numerically solve the model equations. Simulation results are illustrated in Section 8 and

 doi:10.20944/preprints202606.0250.v1



analyzed in Section 9. Concluding remarks are drawn in Section 10 while Appendix A contains the numerical values of model parameters used in the computations.

## 2. Physiology of AH Dynamics

Figure 1 is a multiscale view of the human eye focusing on the regions that are involved in the process of AH dynamics. The leftmost panel is a cross-section of the eye in the sagittal plane. The panel in the center of the figure is an histology of the anterior segment of the eye and shows the frontal portion of the eye occupied by the aqueous humor (anterior chamber, AC), the cornea, the iris, the ciliary body (CB) and the trabecular meshwork (TM). The rightmost panel is a zoomed view of the ciliary body and shows a ciliary process, which is the region of the CB where AH is produced. The ciliary process includes the ciliary capillaries (CC, not shown here), the ciliary stroma (CS) and the cellular double layer constituting the ciliary epithelium (CE). This latter is formed by a couplet of cells facing each other from the apical side, the pigmented epithelial (PE) and nonpigmented epithelial (NPE) cells, respectively. The region indicated with "Aqueous humor" and facing from below the CE is a subset of the posterior chamber (PC). In normal conditions, AH flows out of the CCs throughout fenestrations located on the capillary surface; then, it traverses the CS and the CE, which filters out the solutes with large molecular weight (including blood particles); eventually, the produced aqueous fluid flows along the PC until it reaches the AC. In its final course, AH exits the AC for further recirculation into the CCs by means of the TM and uveoscleral (UV) outflow pathways. In the case of the TM pathway, AH percolates through the multi-layered porous structure of the TM tissue from which it enters the Schlemm's canal and eventually drains into the episcleral vein (EV). In the case of the UV pathway, AH diffuses through the ciliary muscle bundles into the suprachoroidal space (SCS) from which it drains into the choroidal vessels (see [19]).

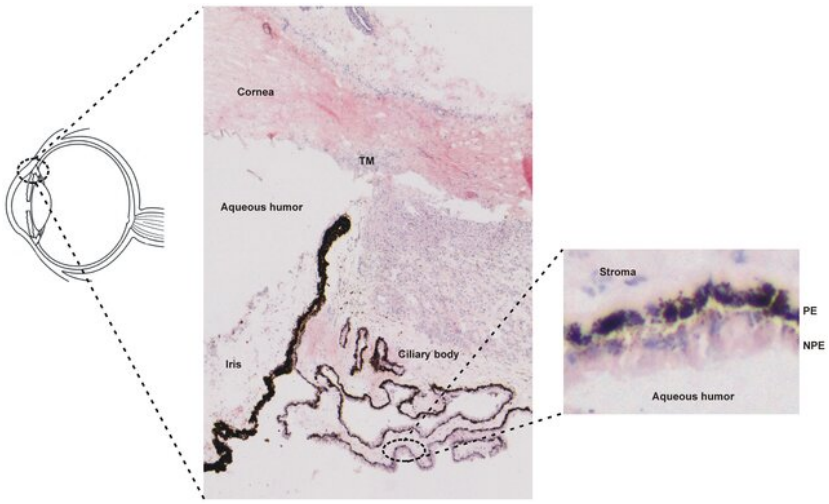


**Figure 1.** Multiscale view of the regions of the eye involved in AH dynamics. Reprinted with permission from [18]. Copyright 2012 Authors, licensed under a Creative Commons Attribution (CC BY) license.

## 3. Fluid and Solute Transport Across a Semipermeable Membrane

The description in Section 2 shows that AH travels across six biological semipermeable membranes (SM) during its flow from the CB to the TM and UV outflow pathways. The first membrane is the wall of the fenestrated CCs. The second and third membranes are the basement membranes separating the CE from the CS and PC, respectively. The fourth membrane is the pupil separating the PC from the AC. The fifth and sixth membranes are the porous structures of the TM and ciliary muscle, respectively. In the next sections we introduce a mathematical representation of AH flow across a biological membrane and its interpretation using the analogy between fluid and electric variables.

 doi:10.20944/preprints202606.0250.v1



### 3.1. Starling's Law of Ultrafiltration

Let $a$ and $b$ denote two compartments separated by a SM $\mathcal{M}_{ab}$ and $U$ a physical variable with values $U_a$ and $U_b$ in $a$ and $b$, respectively, with $\Delta U := U_a - U_b$. Fluid and solute transport across $\mathcal{M}_{ab}$ can be mathematically described using Starling's law of ultrafiltration (see [20] and [21])

$$Q_{\mathrm{ab}} = C_{\mathrm{ab}} \Delta \mathcal{P}. \tag{1a}$$

The quantities $Q_{\mathrm{ab}}$ and $C_{\mathrm{ab}}$ are the AH VFR across $\mathcal{M}_{ab}$ and the facility of $\mathcal{M}_{ab}$, respectively, whereas

$$\mathcal{P} := p - \Pi \tag{1b}$$

is the total pressure, given by the difference between the hydraulic pressure $p$ and the electro-osmo-oncotic (EOO) pressure $\Pi$, which is defined in the next section.

### 3.2. Electro-Osmo-Oncotic Pressure

AH is a homogeneous mixture constituted by water, charged solutes (ions) and neutral solutes (see [8, Chapters 13, 26]). We denote by $S_\alpha$ and $S_\beta$ the sets containing the labels of ions and neutral solutes, respectively; for each $\alpha \in S_\alpha$, $c_\alpha$ and $z_\alpha$ are the molar density and charge number of ion $\alpha$, respectively; for each $\beta \in S_\beta$, $c_\beta$ is the molar density of neutral solute $\beta$; finally, $c_{\mathrm{X}}$ is the molar density of the impermeant protein charge which ensures the electroneutrality of the AH solution. For each $\alpha \in S_\alpha$ and $\beta \in S_\beta$, the quantities $\sigma_\alpha$ and $\sigma_\beta$ are the reflection coefficients of ion $\alpha$ and neutral solute $\beta$ associated with the SM, respectively. Both $\sigma_\alpha$ and $\sigma_\beta$ range in $[0, 1]$, with $\sigma_\alpha$ ($\sigma_\beta$) being close to 0 or 1 if the SM is highly permeable or impermeant to the considered ion (solute), respectively, implying that $\sigma_{\mathrm{X}} = 1$. The EOO pressure difference between compartments $a$ and $b$ is defined as follows(see [22])

$$\Delta\Pi = F \sum_{\alpha \in S_\alpha} \sigma_\alpha z_\alpha \langle c_\alpha \rangle \Delta \varphi_\alpha^{\mathrm{ec}} + RT \sum_{\beta \in S_\beta} \sigma_\beta \Delta c_\beta + RT \sigma_{\mathrm{X}} \Delta c_{\mathrm{X}}, \tag{2a}$$

where $F$ and $R$ are Faraday and gas constants, respectively, $T$ is the absolute temperature of the system, $\langle c_\alpha \rangle = (c_{\alpha,a} + c_{\alpha,b})/2$ and for each $\alpha \in S_\alpha$ the quantity

$$\varphi_\alpha^{\mathrm{ec}} = \psi + \frac{R\,T}{F\,z_\alpha} \ln\left(\frac{c_\alpha}{c_{\mathrm{ref}}}\right) \tag{2b}$$

is the electrochemical potential of ion $\alpha$, with $\psi$ and $c_{\mathrm{ref}}$ denoting the electric potential and the ion reference molar density, respectively.

### 3.3. The Starling Resistor

Leveraging the analogy between electric and fluid variables (see [8, Chapter 15]), we illustrate in Figure 2 the pictorial representation of equations (1). The left panel of Figure 2 is a scheme of the physical system constituted by a SM $\mathcal{M}_{ab}$ separating two compartments $a$ and $b$ containing a homogeneous solution constituted by water, ions and neutral solutes. The right panel of Figure 2 is a scheme of the "Starling resistor", constituted by the electric conductance $C_{ab}$ connecting two nodes of a circuit, denoted by $a$ and $b$. Based on this electric equivalent scheme, we see that equation (1a) can be regarded as a generalized Ohm's law in which the electric current $Q_{ab}$ flowing across a resistor is proportional to the voltage $V := \Delta\mathcal{P}$. Interestingly, using the definition (1b) we see that the AH VFR is the sum of two terms, whose difference expresses the physical fact that AH water flow due to the EOO pressure difference has an opposite direction with respect to AH water flow due to the hydraulic pressure difference.

 doi:10.20944/preprints202606.0250.v1



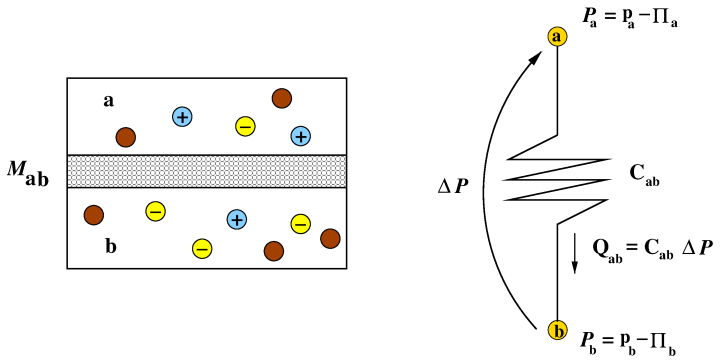


**Figure 2.** Left panel: compartments $a$ and $b$ separated by a SM $\mathcal{M}_{ab}$. The yellow and blue circles represent monovalent anions and cations, respectively, while the brown circles represent a neutral solute. Right panel: electric equivalent representation of Starling's law of ultrafiltration across $\mathcal{M}_{ab}$.

## 4. Electric Equivalent Scheme of AH Dynamics

Figure 3 is the electric equivalent representation of the anterior segment of the eye and of the three main processes that characterize AH dynamics. M1, M2 and M3 are AH production, passive flow and drainage modules, respectively. The black arrows indicate the communication between modules and the circles are the nodes of the electric equivalent circuit. The red circles are the nodes where the dependent variables of the model are given quantities while the numbered yellow circles are the nodes of the circuit where the dependent variables of the model must be computed.

**Assumption 1** (Input data for the EOO). *The EOO $\overline{\Pi}_{CC}$ is given and equal to $\Pi_{bp}$, where $\Pi_{bp}$ is computed using (2) in which the values of electric potential and solute molar densities are measured in the blood plasma. The EOOs $\overline{\Pi}_{EV}$ and $\overline{\Pi}_{EV}$ are given and equal to $\Pi_{aq}$, where $\Pi_{aq}$ is computed using (2) in which the values of electric potential and solute molar densities are measured in the aqueous side. The EOO at the nodes ②, ③, ④ and ⑤ is equal to $\Pi_{aq}$.*

 doi:10.20944/preprints202606.0250.v1



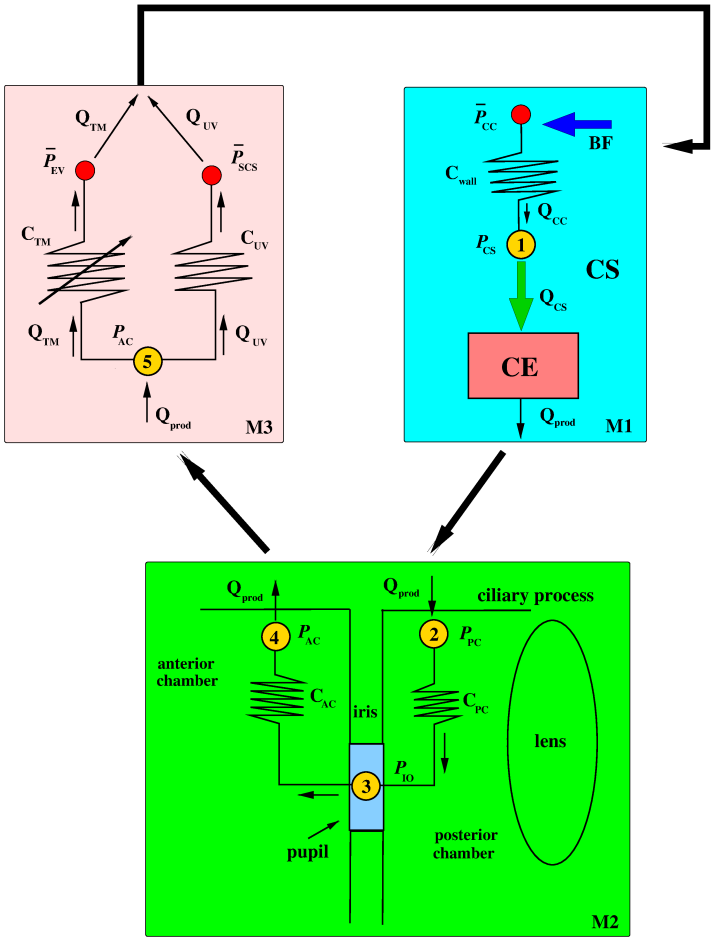


**Figure 3.** Modular representation of the anterior segment of the eye. The quantities $\overline{\mathcal{P}}_{\mathrm{CC}}$, $\overline{\mathcal{P}}_{\mathrm{EV}}$ and $\overline{\mathcal{P}}_{\mathrm{SCS}}$ denote given values of the total pressure at the compartments CC, EV and SCS, respectively.

The blue arrow labeled "BF" represents blood flow transporting the "metabolic fuel" necessary for the production of the aqueous watery fluid indicated by the green arrow (see [10]). The block labeled "CE" represents the cellular scale mechanisms occurring in the CE. Assumption 1 implies that passive AH flow throughout the PC and AC, as well as AH flow throughout the UV outflow pathway, is described by the fluid analog of Ohm's law which is obtained by setting $\Delta\Pi = 0$ in (1). $C_{\mathrm{PC}}$, $C_{\mathrm{AC}}$, $C_{\mathrm{TM}}$ and $C_{\mathrm{UV}}$ are the hydraulic conductances (referred to as "facilities") of the PC, AC and of the TM and UV outflow pathways, respectively. The black arrow across $C_{\mathrm{TM}}$ indicates that the TM facility depends nonlinearly on the pressure difference $p_{\mathrm{AC}} - \overline{p}_{\mathrm{EV}}$. $Q_{\mathrm{CC}}$ is the AH VFR that filtrates across the fenestrated CCs into the CS whereas $Q_{\mathrm{CS}}$ is the AH VFR that travels between the CS and reaches the CE. $Q_{\mathrm{prod}}$ is the AH VFR that is produced by module M1 whereas $Q_{\mathrm{TM}}$ and $Q_{\mathrm{UV}}$ are the AH VFRs drained out by TM and UV outflow pathways, respectively.

## 5. Multiscale Mathematical Model of AH Dynamics

In this section we illustrate the equations that constitute the mathematical model of AH dynamics at the macroscale and microscale levels.

 doi:10.20944/preprints202606.0250.v1



### 5.1. Macroscale Equations

Referring to the circuit illustrated in Figure 3, the application of Kirchhoff current law (KCL) at node ①, the continuity of current across block CE, and the application of KCL at nodes ②, ③, ④ and ⑤ give rise to the following set of algebraic equations:

$$-C_{\text{wall}}\left[\overline{\mathcal{P}}_{\text{CC}}-\mathcal{P}_{\text{CS}}\right]+Q_{\text{CS}}=0, \tag{3a}$$

$$-Q_{\text{CS}}+Q_{\text{prod}}=0, \tag{3b}$$

$$-Q_{\text{prod}}+C_{\text{PC}}[\mathcal{P}_{\text{PC}}-\mathcal{P}_{\text{IO}}]=0, \tag{3c}$$

$$-C_{\text{PC}}[\mathcal{P}_{\text{PC}}-\mathcal{P}_{\text{IO}}]+C_{\text{AC}}[\mathcal{P}_{\text{IO}}-\mathcal{P}_{\text{AC}}]=0, \tag{3d}$$

$$-C_{\text{AC}}[\mathcal{P}_{\text{IO}}-\mathcal{P}_{\text{AC}}]+Q_{\text{prod}}=0, \tag{3e}$$

$$-Q_{\text{prod}}+Q_{\text{TM}}+C_{\text{UV}}\left[\mathcal{P}_{\text{AC}}-\overline{\mathcal{P}}_{\text{SCS}}\right]=0. \tag{3f}$$

System (3) is the macroscale model of AH dynamics and consists of six algebraic equations for seven dependent variables, comprising three VFRs: $Q_{\text{CS}}$, $Q_{\text{prod}}$ and $Q_{\text{TM}}$, and four pressures: $\mathcal{P}_{\text{CS}}$, $\mathcal{P}_{\text{PC}}$, $\mathcal{P}_{\text{IO}}$ and $\mathcal{P}_{\text{AC}}$.

### 5.2. The Unit Cell of the CE

Figure 4 shows the compartment subdivision of the "unit cell" whose periodic repetition represents the CE. White circles indicate the number of the compartment whereas white rectangles indicate the number of the interface separating two neighbouring compartments. The compartment numbered ① is the CS. The compartments numbered ② and ④ and indicated by "1/2 PE cell" and "1/2 NPE cell", respectively, correspond to one half of each PE and NPE cell. The compartments numbered ③ and ⑤ and indicated by "1/2 PE pc" and "1/2 NPE pc", respectively, correspond to one half of the paracellular (pc) spaces separating couplets of PE and NPE cells. The compartment numbered ⑥ is the PC. The rectangle in purple color is the BM and has a thickness equal to $t_{\text{BM}}$. The rectangular boundary in light green color surrounding compartments numbered ② and ④ is the BLM and has a thickness equal to $t_{\text{BL}}$. The rectangle in gold color is the GJ separating the PE and NPE cells whereas the rectangle with a porous pattern is the TJ separating the paracellular spaces ③ and ⑤. Since the CE is a "leaky epithelium" (see [23,24]) the TJ allows the passage of water, ions and low molecular weight (MW) molecules and does not allow the passage of large MW molecules. This is the reason why the AH watery fluid has a low content of proteins. The quantities $a$, $b$ and $c$ are the length of the sides of the various compartments.

 doi:10.20944/preprints202606.0250.v1



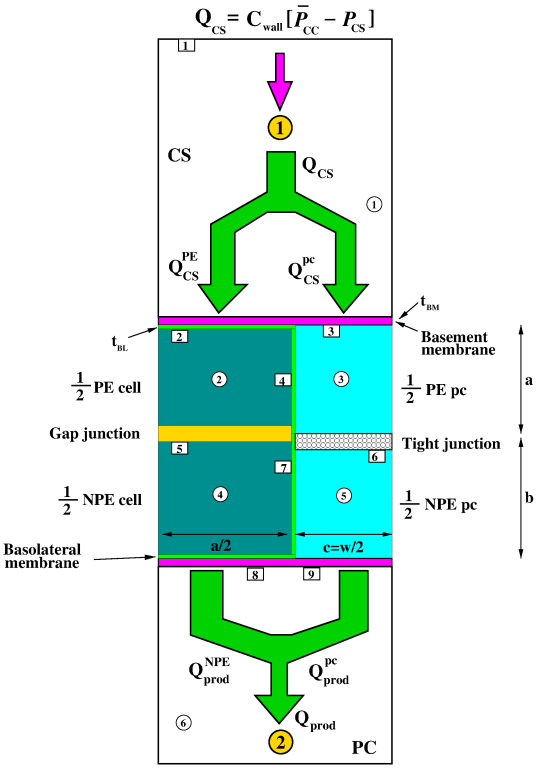


**Figure 4.** Cross-sectional representation of the compartment subdivision of the "unit cell" of the CE.

*5.3. Micro- to Macroscale Model of the CE*

The input to the unit cell is $Q_{CS}$ and the output from the unit cell is $Q_{prod}$. Both quantities depend on the compartment distribution of the electric potential and of each physical constituent of the metabolic fuel of AH dynamics, namely, moving charged solutes (ions), fixed charged solutes (electroneutralizing charged proteins) and moving neutral solutes (low to medium-high molecular weight molecules). To couple the microscale representation of the CE with $Q_{CS}$ and the micro- to macroscale models for $Q_{prod}$ described in Section 5.4, respectively, we write the mass balance equations for water and solutes in each compartment of the unit cell (see [8, Chapter 7]). Denoting by $u$ any of the problem physical variables, the stationary mass balance of $u$ is described by the following partial differential equation (PDE)

$$\nabla \cdot \mathbf{F} = \mathcal{G} - \mathcal{C}, \tag{4a}$$

The quantity $\mathbf{F}$ is the flux density of $u$ whereas $\mathcal{G}$ and $\mathcal{C}$ are the production and consumption rates of $u$ (possibly depending on $u$). Denoting by $\Omega_i$, $i = 1, \ldots, 5$, the $i$-th compartment in the scheme of Figure 4, integrating both sides of (4a) over $\Omega_i$ and applying the divergence theorem to the left-hand side yields the following mass balance equation in integral form

$$\int_{\Sigma_i} \mathbf{F} \cdot \mathbf{n}\, d\Sigma = \int_{\Omega_i} (\mathcal{G} - \mathcal{C})\, d\Omega \qquad i = 1, \ldots, 5, \tag{4b}$$

The left-hand side of (4b) is the net flux of $u$ across the boundary surface $\Sigma_i$ whereas the right-hand side of (4b) is the net production rate of $u$ inside the volume $\Omega_i$. Let us denote by $\mathcal{A}_i$ the index set of the compartments adjacent to $\Omega_i$ and define $\Sigma_{ij} = \Sigma_i \cap \Sigma_j$. Let us replace $\mathbf{F} \cdot \mathbf{n}$ by its value $F_{ij}$ at the centroid of $\Sigma_{ij}$ and assume that $F_{ij}$ depends on $u_i$, $u_j$ and on other quantities, with $u_i$, $u_j$ denoting the values of $u$ at the centroids of $\Omega_i$ and $\Omega_j$, respectively. Finally, let us replace $\mathcal{G}$ and $\mathcal{C}$ by their values $\mathcal{G}_i$

 doi:10.20944/preprints202606.0250.v1



and $\mathcal{C}_i$ at the centroid of $\Omega_i$, with the assumption that $\mathcal{G}_i$ and $\mathcal{C}_i$ may depend on $u_i$. Then, the integral mass balance equation (4b) becomes

$$\sum_{j\in\mathcal{A}_i} F_{ij}(u_i,u_j)|\Sigma_{ij}| = (\mathcal{G}_i(u_i) - \mathcal{C}_i(u_i))|\Omega_i| \qquad i = 1,\dots,5, \tag{4c}$$

where $|\Sigma_{ij}|$ and $|\Omega_i|$ denote the area of $\Sigma_{ij}$ and the volume of $\Omega_i$, respectively. For given values of $u$ in the CC and PC, equations (4c) represent a nonlinear system of algebraic equations for the numerical approximation $\mathbf{U} = [u_1,\, u_2,\, u_3,\, u_4,\, u_5]^T$ of the mean values of $u$ in each compartment $\Omega_i$, $i = 1,\dots,5$.

### *5.4. Micro- to Macroscale Model of $Q_{prod}$*

**Assumption 2** (Total pressure in the PC)**.** *In this section, $\mathcal{P}_{\text{PC}}$, representing the total pressure in the PC, is a given quantity.*

Once the equations (4c) are solved for $i = 1,\dots,5$, the AH VFR produced by the CE can be computed as

$$Q_{\text{prod}} = 2N_{\text{cells}}\left[Q^{\text{NPE}}_{\text{prod}} + Q^{\text{pc}}_{\text{prod}}\right]. \tag{5a}$$

The quantity $N_{\text{cells}}$ denotes the number of NPE cells contained in the CE while the micro- to macroscale model for the AH VFR produced by the NPE cell, $Q^{\text{NPE}}_{\text{prod}}$, and by the paracellular space neighbouring the NPE cell, $Q^{\text{pc}}_{\text{prod}}$, is represented by Starling's law as in (1a):

$$Q^{\text{NPE}}_{\text{prod}} = C_{\boxed{8}}\Delta\mathcal{P}_{\boxed{8}} = C_{\boxed{8}}\left[\mathcal{P}_{④} - \mathcal{P}_{\text{PC}}\right], \tag{5b}$$

$$Q^{\text{pc}}_{\text{prod}} = C_{\boxed{9}}\Delta\mathcal{P}_{\boxed{9}} = C_{\boxed{9}}\left[\mathcal{P}_{⑤} - \mathcal{P}_{\text{PC}}\right], \tag{5c}$$

where $C_{\boxed{8}}$ and $C_{\boxed{9}}$ are the facility of the membranes separating the NPE and the paracellular space neighbouring the NPE cell from the PC, respectively.

### *5.5. Micro- to Macroscale model of $C_{TM}$ and $Q_{TM}$*

Following [25], we assume that at the microscale level the TM can be described as a porous material of thickness $t_{\text{TM}}$ comprised of a solid and fluid constituents, in which the porous structure consists of a collection of $N_p$ parallel circular, cylindrical pores of diameter $d_p$. The TM hydraulic resistance $R_{\text{TM},0}$ can be related to the TM permeability $\kappa_{\text{TM}}$ by Darcy's law as

$$R_{\text{TM},0} = \frac{\mu_{\text{fl}} t_{\text{TM}}}{\kappa_{\text{TM}} A_{\text{TM}}}, \tag{6a}$$

where $\mu_{\text{fl}}$ is the dynamic viscosity of the fluid, $A_{\text{TM}}$ is the total surface of the TM in contact with the AC and

$$\kappa_{\text{TM}} = \frac{\Phi_{\text{TM}} d_p^2}{16\, c_K}, \tag{6b}$$

having denoted by $\Phi_{\text{TM}}$ and $c_K$ the porosity of the TM and the Kozeny constant, respectively. Experimental data shown in [26] suggest that the hydraulic resistance exerted by the TM is not constant but increases linearly with the total pressure difference $X_{\text{TM}} := \mathcal{P}_{\text{AC}} - \overline{\mathcal{P}}_{\text{EV}}$ according to the following relation

$$R_{\text{TM}}(X_{\text{TM}}) = R_{\text{TM},0}\left[1 + \alpha_Q\, X_{\text{TM}}\right], \tag{6c}$$

 doi:10.20944/preprints202606.0250.v1



where $\alpha_Q$ is a nonnegative parameter representing the obstruction coefficient. Taking the reciprocal of (6c) gives the following mathematical model for the TM outflow facility

$$C_{\mathrm{TM}}(X_{\mathrm{TM}}) = \frac{C_{\mathrm{TM},0}}{1 + \alpha_Q\, X_{\mathrm{TM}}}, \tag{6d}$$

where $C_{\mathrm{TM},0} := (R_{\mathrm{TM},0})^{-1}$. The element with the transverse black arrow in module M3 of Figure 3 is the equivalent electric representation of the nonlinear TM outflow facility (6d). The micro- to macroscale model of the AH VFR throughout the TM is given by the following nonlinear Starling's law of ultrafiltration

$$Q_{\mathrm{TM}}(\mathcal{P}_{\mathrm{AC}}) = C_{\mathrm{TM},0}\frac{[\mathcal{P}_{\mathrm{AC}} - \overline{\mathcal{P}}_{\mathrm{EV}}]}{1 + \alpha_Q[\mathcal{P}_{\mathrm{AC}} - \overline{\mathcal{P}}_{\mathrm{EV}}]}. \tag{6e}$$

The nonlinear Ohm's law (6e) reduces to the linear Ohm's law by setting $\alpha_Q = 0$.

## 6. Cellular Mechanisms in AH Production

Figure 5 provides a schematic description of the membrane proteins that allow the exchange of neutral solutes, charged solutes (ions) and water between neighbouring compartments and of the main metabolic activities and chemical reactions occurring in the cytoplasm of the PE and NPE cells. The scheme is an extension of that proposed in [10] and [29] and includes two types of regulatory mechanisms of ion transport across a semipermeable membrane:

1. passive transport mechanisms;
2. active transport mechanisms.

Passive transport is mediated by ion channels (magenta color in Figure 5) and is directed along the electrochemical gradient across the membrane. Active transport is directed against the electrochemical gradient across the membrane and is divided into primary and secondary depending on the type of energy source and the way adopted by the transporter protein to exploit it. Primary active transport is mediated by the Na+/K+ ATPase (also referred to as ionic pump, dark grey color in Figure 5) which directly exploits the ATP produced by the mitochondria (yellow color in Figure 5). Secondary active transport is mediated by the co-transporters (white color circles and ellipse in Figure 5) which indirectly exploit the potential energy source due to the transmembrane concentration gradient of another ion or by the action of specific enzymes such as the Carbonic Anhydrase (CA). Intracellular metabolism of mitochondria regulates the function of cellular respiration. Mitochondria activity is driven by the absorption of glucose and produces carbon dioxide ($CO_2$) and ATP. $CO_2$ is rapidly eliminated from the cytoplasm by the hydrolysis reaction catalyzed by the CA. ATP is used by the $Na^+/K^+$ ATPase to extrude sodium ions from the cell and intrude potassium ions into the cell. Water transport across the various membranes in the scheme of Figure 5 follows two different pathways [30]:

1. passive transport of water molecules (diffusion) across the lipid bilayer of the plasma membrane and the extracellular matrix constituents of the basement membrane;
2. active transport of water molecules across the pores of specialized membrane proteins (aquaporins, AQP) driven by hydraulic-osmotic pressure gradients (facilitated diffusion).

AQPs (green color in Figure 5) are solely expressed on the BLM of the NPE cells which are, as a consequence, responsible of the large majority of AH production by the ciliary processes (see [24] and [27]).

 doi:10.20944/preprints202606.0250.v1



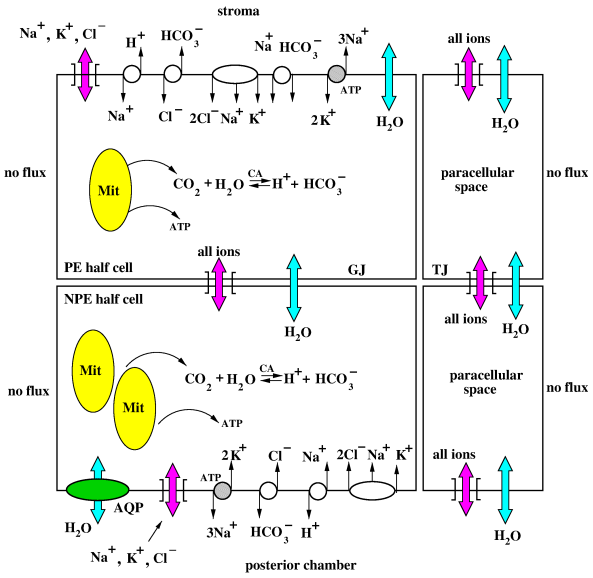


**Figure 5.** Schematic representation of the expression of exchangers of charged solutes and water along the BLM of the PE and NPE cells and on the BM. CA: carbonic anhydrase. AQP: aquaporin. AQPs are expressed on the BLM of the NPE half cell [27], but transepithelial water transport may occur also across the BLM of the PE half cell due to the mediation of the Na+/K+/2Cl- cotransporter [28], the BM and, partly, the TJ separating the paracellular spaces. Mit: mitochondria. ATP: adenosine thriphosphate. Nonpigmented cells contain many more mitochondria than pigmented cells so that a higher degree metabolic activity is likely to occur in the NPE half cell than in the PE half cell [24].

## 7. Solution Map

The computation of the nodal pressures and AH VFRs represented in the scheme of Figure 3 requires the solution of the *fully coupled multiscale model* of AH dynamics (FCMM), consisting of the union of the macroscale equations (3) with the micro- to macroscale equations (5) and (6). The complexity of solving the FCMM lies in the fact that the micro- to macroscale equations depend on the solution at the cellular level of the system of microscale equations (4c) for each constituent of the AH watery fluid (water, moving neutral and charged solutes, immobile charged solutes and electric potential). To end up with a numerical procedure that is manageable for research and clinical applications, we propose in the present work a solution map (or functional iteration, see [31], [8, Chapter 21]), which consists of transforming the task of solving the FCMM into the successive solution of problems of lower dimension until convergence. The solution map is illustrated in Algorithm 1 where $\mathbf{X} = [\mathcal{P}_{\mathrm{CS}}, \mathcal{P}_{\mathrm{PC}}, \mathcal{P}_{\mathrm{IO}}, \mathcal{P}_{\mathrm{AC}}]^T$, $\|\mathbf{W}\|_\infty := \max_{i=1,\dots,n} |W_i|$ for any $\mathbf{W} \in \mathbb{R}^n$, and the superscript $()^*$ identifies the approximate solution of the FCMM at convergence. Notice that for $k > 0$, the initial guess $\mathbf{X}^{(0)}$ for the $k+1$-th iteration of the solution map is the linear interpolation of the last computed iterate $\mathbf{X}^{(k+1)}$ and the previous iterate $\mathbf{X}^{(k)}$ by means of a relaxation parameter $\theta$ to be chosen in the interval $(0, 1]$.

## 8. Results

In this section we illustrate the outcome of a series of simulations aiming at:

1. to identify the optimal value of the relaxation parameter $\theta$;
2. to investigate the impact of a differential expression of the $Na^+$ ionic channels along the BLM of the PE and NPE cells on the production of AH by the CE;
3. to investigate the impact of $\alpha_Q$ and $p_{\mathrm{ev}}$ on the formation of the IOP and on the drainage of AH by the TM and UV outflow pathways.

Our final goal is to leverage the results from items 2. and 3. to better understand the pathological dysfunctions behind severe ocular diseases such as primary open angle glaucoma and/or thyroid eye disease and to help design patient-specific pharmacological therapies.

 doi:10.20944/preprints202606.0250.v1



**Algorithm 1** Solution map for the FCMM

1: Provide an initial datum $\mathbf{X}^{(0)}$ and a tolerance `tol`.
2: Set $k = 0$.
3: Set $\mathcal{P}_{\mathrm{PC}} = \mathcal{P}_{\mathrm{PC}}^{(k)}$ and solve the system formed by the union of equations (3a), (3b) and (4c).
4: Compute $y^{(k+1)} = Q_{\mathrm{prod}}^{(k+1)}$ using equation (5a).
5: Set $Q_{\mathrm{prod}} = y^{(k+1)}$ and solve the system formed by equations (3c), (3d), (3e), (3f) and (6e).
6: Compute $\delta\mathbf{X}^{(k)} = \mathbf{X}^{(k+1)} - \mathbf{X}^{(k)}$ and compute the relative increment between two consecutive iterations

$$\epsilon^{(k)} = \frac{\|\delta\mathbf{X}^{(k)}\|_\infty}{\|\mathbf{X}^{(k+1)}\|_\infty}. \tag{7}$$

7: **if** $\epsilon^{(k)} <$ `tol` **then**
8: Set $\mathbf{X}^* = \mathbf{X}^{(k+1)}$.
9: Compute $Q_{\mathrm{prod}}$ using equation (5a) and set $Q_{\mathrm{prod}}^* = Q_{\mathrm{prod}}$.
10: Compute $Q_{\mathrm{TM}}$ using equation (6e) and set $Q_{\mathrm{TM}}^* = Q_{\mathrm{TM}}$.
11: Set $Q_{\mathrm{UV}}^* = Q_{\mathrm{prod}}^* - Q_{\mathrm{TM}}^*$.
12: Exit.
13: **else**
14: $\mathbf{X}^{(0)} = \theta\mathbf{X}^{(k+1)} + (1-\theta)\mathbf{X}^{(k)}$;
15: $k \leftarrow k+1$;
16: go to line 2.
17: **end if**

### *8.1. Model Calibration in Baseline Conditions*

In this section we perform a calibration of the set of model parameters in such a way that under given physiological values of the boundary data, Algorithm 1 returns approximations to $Q_{\mathrm{prod}}$ and $p_{\mathrm{IO}}$ that are as close as possible to the baseline values for healthy control subjects $Q_{\mathrm{prod,b}} = 2.75\mu\mathrm{Lmin}^{-1}$ and $p_{\mathrm{IO,b}} = 15\mathrm{mmHg}$ indicated in the seminal references [1] and [10].

Following [10], we set $\overline{p}_{\mathrm{CC}} = 25\mathrm{mmHg}$ and $\overline{p}_{\mathrm{ec}} = 8\mathrm{mmHg}$; following [32], we set $\overline{p}_{\mathrm{scs}} = 11\mathrm{mmHg}$; we also set $p_{\mathrm{PC}}^{(0)} = 0\mathrm{mmHg}$, $\theta = 0.8$, the obstruction coefficient $\alpha_Q = 0\mathrm{mmHg}^{-1}$ and $\mathtt{tol} = 10^{-8}$. The values of the other main model parameters are reported in Appendix A. A screenshot of the output of the computer code at convergence is illustrated in Figure 6. The percentage discrepancy between the calculated values of $Q_{\mathrm{prod}}$ and $p_{\mathrm{IO}}$ and the baseline values $Q_{\mathrm{prod,b}}$ and $p_{\mathrm{IO,b}}$ is 0.0060 % and 0.0026 %, respectively.

Figure 7 shows a pictorial view of the pathway followed by AH water flow in its motion across the CE towards the aqueous side in the PC. We see that AH flows from the stroma along parallel directions, one intercellularly from half-PE to half-NPE cell, the other from the paracellular space neighbour to the half-PE cell to the paracellular space neighbour to the half-NPE cell. We also see that no water flow is predicted to be exchanged between the half-cells of the CE and the neighbour paracellular space.

Preprints.org (www.preprints.org) | NOT PEER-REVIEWED | Posted: 3 June 2026 doi:10.20944/preprints202606.0250.v1



```
-----------------------------------------
# of iterations               = 23
relative error on PC pressure = 1.00123e-09
-----------------------------------------

          ascorbate     glucose       lactate       urea    [mM]
CC          0.0400      5.9000        1.9000       7.3000
st          0.4287      4.7187        2.2430       6.8427
PE          0.8133      3.5498        2.5823       6.3902
pc/PE       0.8133      3.5498        2.5823       6.3903
NPE         0.8586      3.4122        2.6223       6.3370
pc/NPE      0.8586      3.4122        2.6223       6.3370
PC          1.0600      2.8000        2.8000       6.1000

            Na+          K+          pH          Cl-         HCO3-     [mM]
CC        148.0000    4.5700      7.4000     107.0000     26.0000
st        148.4431    4.3180      7.0909     117.1476     27.2635
PE        148.9011    4.0668      7.1454     127.0913     31.0477
pc/PE     148.9012    4.0668      7.1427     127.0907     30.8486
NPE       151.0249    4.0934      7.1388     126.5056     30.5802
pc/NPE    151.0249    4.0934      7.1330     126.5056     30.1775
PC        152.0000    3.9800      7.2100     131.0000     22.0000

       pressure [mmHg]     potential [mV]     fixed charges [mM]     zX
CC          25.000               1.200              19.570           -1
st          22.001               0.338               8.350           -1
PE          21.005              -0.612               5.171            1
pc/PE       21.005              -0.600               4.971            1
NPE         19.007              -0.322               1.967            1
pc/NPE      19.007              -0.296               1.565            1
PC          16.000               0.000               2.980           -1
IOP         15.000
AC          14.000
EPI          8.000
SCS         11.000

AH volumetric flow rates [muL/min]
Qprod   =  2.749834
Q_TM    =  2.449867
Q_UV    =  0.299967
Q_out   =  2.749834
```

**Figure 6.** Screen output summarizing the main quantities computed by Algorithm 1 in baseline conditions.

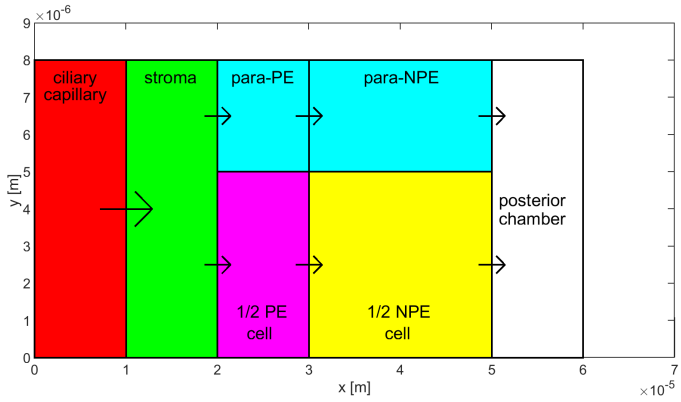


**Figure 7.** This figure illustrates the distribution of normal velocities of AH fluid between the various compartments of the unit cell representing the CE.

Figure 8 graphically shows the number of iterations $N_{it}$ required by the fixed-point Algorithm 1 to converge as a function of the relaxation parameter $\theta$. We see that increasing $\theta$ until 0.8 improves the convergence rate; then, furtherly increasing $\theta$ even leads to convergence failure within the maximum allowed number of iterations (equal to 5000).

 doi:10.20944/preprints202606.0250.v1



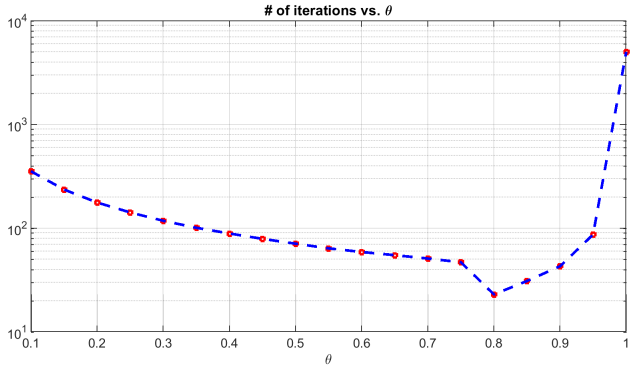


**Figure 8.** Number of iterations $N_{it}$ required by the fixed-point map to converge as a function of the relaxation parameter $\theta$.

*8.2. The Role of the Expression of the $Na^+$ Channels*

In this section we use the model to theoretically support the experimental conclusions reached in [33] regarding the expression of ameloride-sensitive $Na^+$ channels along the BLM of the NPE cells and their role in controlling AH production by the CE. Data shown in [33] demonstrated that the correct unidirecthetional secretion of AH from the stroma to the PC is accompanied by a net release of sodium from the NPE cells into the PC resulting from the balance between sodium extrusion by the Na+/K+ ATPase and sodium reabsorption through the ameloride-sensitive $Na^+$ channels.

To check this important finding, we conducted two numerical simulations: in the first simulation (S1), we ran Algorithm 1 by mathematically setting to zero the value of the diffusional permeability to sodium on the BLM of the sole PE half cell; in the second simulation (S2), we ran Algorithm 1 by mathematically setting to zero the value of the diffusional permeability to sodium **also** on the BLM of the NPE half cell. No difference was detected between the convergence history of the solution map of S1 and that illustrated in Figure 6. Conversely, in the convergence history of the solution map of S2 represented in Figure 9 we see that the predicted value of $Na^+$ molar density in the PE and NPE half cells is equal to zero. This depletion of intracellular sodium leads to a breakdown of water flow and pressure balance in the whole circuit of the anterior segment of the eye, as witnessed by the 'NaN' IEEE arithmetic representation for a "Not-a-Number" obtained as a result of mathematically undefined operations like 0.0/0.0 (see [34]).

 doi:10.20944/preprints202606.0250.v1



```
-----------------------------------------
# of iterations               = 1
relative error on PC pressure = NaN
-----------------------------------------

          ascorbate    glucose       lactate       urea    [mM]
CC          0.0400      5.9000        1.9000       7.3000
st          0.4287      4.7187        2.2430       6.8427
PE          0.8133      3.5498        2.5823       6.3902
pc/PE       0.8133      3.5498        2.5823       6.3903
NPE         0.8586      3.4122        2.6223       6.3370
pc/NPE      0.8586      3.4122        2.6223       6.3370
PC          1.0600      2.8000        2.8000       6.1000

            Na+          K+         pH         Cl-        HCO3-     [mM]
CC        148.0000    4.5700     7.4000    107.0000     26.0000
st        149.4815    4.3180     7.0531    117.1465     43.7278
PE          0.0000    4.0668     7.0374    127.0420     42.0347
pc/PE     149.9504    4.0668     7.0374    127.0415     42.4303
NPE         0.0000    4.0934     7.0128    126.4569     40.3066
pc/NPE    151.0360    4.0934     7.0128    126.4571     39.4001
PC        152.0000    3.9800     7.2100    131.0000     22.0000

       pressure [mmHg]    potential [mV]     fixed charges [mM]    zX
CC             NaN              1.200              19.570          -1
st             NaN              1.085               7.075           1
PE             NaN              0.973             165.010           1
pc/PE          NaN              0.973              15.454           1
NPE            NaN              0.282             162.670           1
pc/NPE         NaN              0.282              10.728           1
PC             NaN              0.000               2.980          -1
IOP            NaN
AC             NaN
EPI          8.000
SCS         11.000

AH volumetric flow rates [muL/min]
Qprod    =       NaN
Q_TM     =       NaN
Q_UV     =       NaN
Q_out    =       NaN
```

**Figure 9.** Screen output summarizing the main quantities computed by Algorithm 1 in the case where there is no expression of $Na^+$ ion channels on the BLM of **both** PE and NPE cells.

### *8.3. The Impact of $\alpha_Q$ and $p_{ev}$*

In this section we conduct a sensitivity analysis with respect to the obstruction coefficient $\alpha_Q$ in (6d) and the pressure in the episcleral vein $p_{\text{ev}}$.

Figure 10 illustrates the distribution of predicted values of IOP in correspondence of 101 values of $\alpha_Q$ equally distributed in the interval $[0,\ 0.2]\text{mmHg}^{-1}$ and for 6 values of $p_{\text{ev}}$ equally distributed in the interval $[8,\ 20]$ mmHg. We see that IOP increases by almost 40 % with respect to baseline conditions, reaching a value of 20.9 mmHg which is very close to the upper limit of 21 mmHg that separates "normal" from "pathological" conditions.

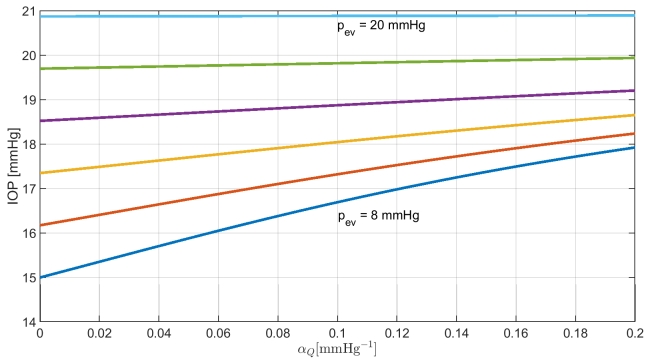


**Figure 10.** Predicted values of IOP as a function of the obstruction coefficient $\alpha_Q$ taken in the interval $[0,\ 0.2]\ \text{mmHg}^{-1}$ and $p_{\text{ev}}$ taken in the interval $[8,\ 20]$ mmHg. The value of the relaxation parameter was $\theta = 0.8$.

Figure 11 illustrates the distribution of predicted values of $Q_{\text{prod}}$ (top panel), $Q_{\text{TM}}$ (middle panel) and $Q_{\text{UV}}$ (bottom panel) in correspondence of the same values of $\alpha_Q$ and $p_{\text{ev}}$ used in Figure 10. We see that the predicted VFRs of produced AH and drained AH through the TM outflow pathway decrease

 doi:10.20944/preprints202606.0250.v1



by almost 60 % and 93 % with respect to baseline conditions, whereas the predicted VFR of drained AH through the UV outflow pathway increases by more than 3 times with respect to baseline conditions.

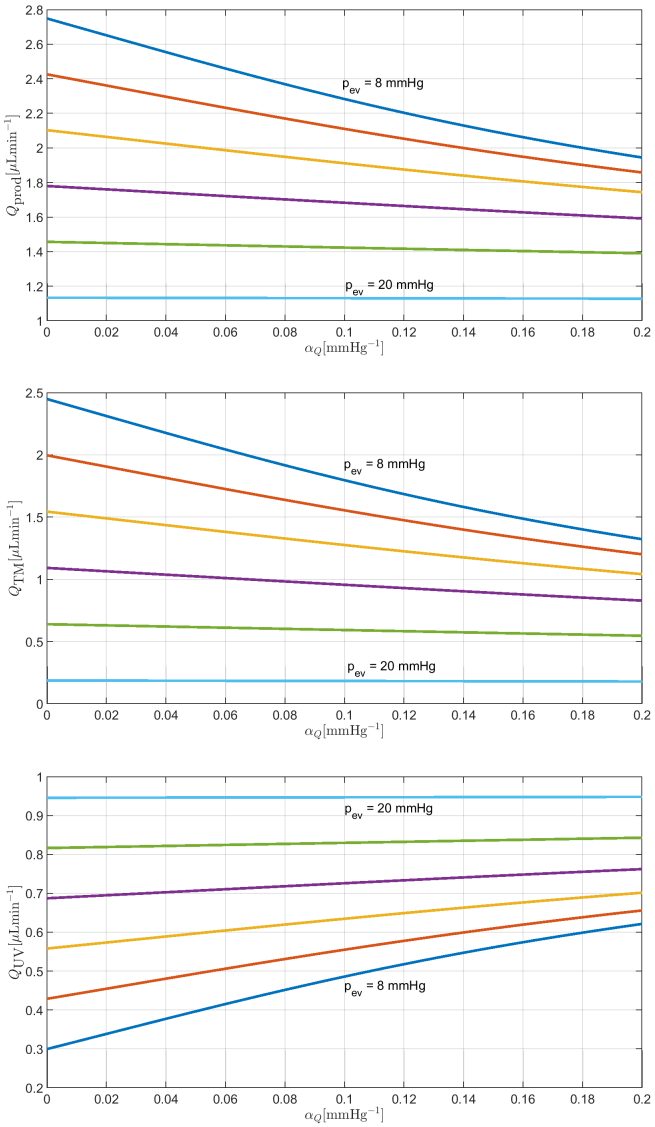


**Figure 11.** Top: $Q_{\text{prod}}$. Middle: $Q_{\text{TM}}$. Bottom: $Q_{\text{UV}}$. The three variables were computed as a function of the obstruction coefficient $\alpha_Q$ taken in the interval $[0, 0.2]$ mmHg$^{-1}$ and $p_{\text{ev}}$ taken in the interval $[8, 20]$ mmHg. The value of the relaxation parameter was $\theta = 0.8$.

## 9. Discussion

The dynamics of AH in the human eye is the focus of extensive experimental and computational research [1,10,13,15,35]. In this study, we developed a modular mathematical model of AH dynamics capable of simulating the processes of production, passive flow and drainage of AH with an equivalent electric circuit of the anterior segment of the eye. The main advantage of the model lies in the integration of multiple spatial scales ranging from $10^{-9}$m to $10^{-2}$m within a 0D representation based on the successive solution of systems of nonlinear algebraic equations of small size. This multiscale modeling approach provides an improved capability to capture how phenomena occurring at levels difficult to access experimentally affect the macroscopic function of the eye. The simulation results demonstrated that: (C1) $Na^+$ channels on the BLM of the NPE cells are necessary to obtain a physiological direction and intensity of AH production; and (C2) the nonlinear dependence of TM outflow facility has a substantial impact on the formation of IOP and AH production. Conclusion C1 is an original contribution of this article because it gives a theoretical confirmation of the experimental findings

 doi:10.20944/preprints202606.0250.v1



of [33] about the pivotal role of sodium reabsorption to compensate excessive sodium extrusion due to the action of the sodium/potassium pump on the BLM of NPE cells. Conclusion C2 is another original contribution of this article and has a twofold valence. On the one hand, it extends the range of application of the nonlinear model of TM outflow resistance proposed in [26] to the simulation of the whole process of AH dynamics. On the other hand, it allows us to parametrically investigate the pressure condition of the eye and the rate of AH production with respect to the variation of the obstruction coefficient $\alpha_Q$ and episcleral vein pressure $\overline{p}_{\text{ev}}$. Results support the conjecture that deterioration of the TM tissue poroelastic properties due to aging and molecular-driven dysfunctions of TM cells may be directly related to an increase of IOP to levels compatible with primary open angle glaucoma development (see [36–38]). Results also support the conjecture that Thyroid Eye Disease (TED) may cause secondary glaucoma because of compression of the ophthalmic veins which results into an increase of the episcleral venous pressure and, in turn, of IOP (see [4,5,39]). Finally, results support the conjecture raised in [40] that the UV outflow pathway acts as a "relief valve" when the TM outflow pathway fails at appropriately draining AH out of the AC. We can verify this conclusion by comparing the middle and bottom panels of Figure 11 which show that $Q_{\text{TM}}$ progressively decreases with $\alpha_Q$ and $p_{\text{ev}}$ while $Q_{\text{UV}}$ progressively increases.

## 10. Conclusions

In this article, we developed a compartment-based mathematical model of AH dynamics in the human eye, consisting of three modules (M1, M2 and M3) which describe at a macroscopic scale the processes of AH production, passive flow and drainage.

We used the model to comprehend how the findings of each module may help to explain the onset and progression of an ocular disease and to evaluate their impact on patient's health by contributing to develop specifically targeted therapeutical approaches. In particular, we investigated the role of (1) sodium channels in AH production and (2) episcleral vein pressure in AH drainage. Model predictions suggest that (1) the expression of sodium channels in the NPE cells of the CE is essential for AH to flow from the ciliary processes into the posterior chamber; and (2) an increase of the episcleral vein pressure reduces AH drainage, potentially explaining the development of secondary open-angle glaucoma.

Compared to existing compartment models, our formulation is characterized by a genuine multiscale nature because M1 and M3 incorporate cellular-scale mechanisms which are difficult to access experimentally though significantly impacting the functions of the eye. The multiscale structure is the point of strength of the model and makes it ideal for use in a clinical setting.

The model is also affected by limitations: (L1) it is restricted to stationary simulations; (L2) it is not connected to the external structures of the anterior chamber, such as the cornea; (L3) it is not connected to the posterior structures of the eye, such as the retina. While (L1) can be easily overcome by introducing a further loop over the time variable in Algorithm 1, (L2) and (L3) require elaborations which will be the object of the next steps of our research.

**Acknowledgments:** This work was partially supported by NIH grants R01EY030851 and R01EY034718, NSF grants 2108711/2327640 and 2412130, NYEE Foundation grants, The Glaucoma Foundation, and in part by a Challenge Grant award from Research to Prevent Blindness, NY. Professor Alon Harris is supported by NIH grants (R01EY030851 and (R01EY034718), NYEE Foundation grants, The Glaucoma Foundation, and in part by a Challenge Grant award from Research to Prevent Blindness, NY. Dr. Alice Verticchio is supported by NYEE Foundation grant. The funders had no role in the design of the study; in the collection, analyses, or interpretation of data; in the writing of the manuscript; or in the decision to publish the results.

## Appendix A Numerical Values of Model Parameters

The sets of the neutral and charged moving solutes are defined as follows:

$$S_\alpha = \{\text{Na}^+, \text{K}^+, \text{H}^+, \text{Cl}^-, \text{HCO}_3^-\}, \tag{A8a}$$

$$S_\beta = \{\text{ascorbate, glucose, lactate, urea}\}. \tag{A8b}$$

 doi:10.20944/preprints202606.0250.v1



The molar densities, in the plasma and in the aqueous side, of the quantities in (A8) are listed in Table A1, together with the reference publication from which they were taken.

**Table A1.** Molar densities of charged and neutral moving solutes in the plasma and in the aqueous side. For each set of data, the reference article is cited.

| solute | plasma [mM] | aqueous [mM] | ref. |
|---|---|---|---|
| $Na^+$ | 148 | 152 | [41] |
| $K^+$ | 4.57 | 3.98 | [42] |
| $H^+$ | 7.4 (pH) | 7.21 (pH) | [41] |
| $Cl^-$ | 107 | 131 | [41] |
| $HCO_3^-$ 26 | 22 | | [41] |
| ascorbate | 0.04 | 1.06 | [41] |
| glucose | 5.9 | 2.8 | [41] |
| lactate | 1.9 | 2.8 | [41] |
| urea | 7.3 | 6.1 | [41] |

## References


1. Brubaker, R.F. Flow of Aqueous Humor in Humans. *Invest Ophthalmol Vis Sci* **1991**, *32*, 3145–3166.
2. Steinmetz, J.; Bourne, R.; Briant, P.; et al.. Causes of blindness and vision impairment in 2020 and trends over 30 years, and prevalence of avoidable blindness in relation to VISION 2020: the Right to Sight: an analysis for the Global Burden of Disease Study. *Lancet Glob Health* **2021**, *8*, e144–e160.
3. Wang, Y.X.; Xu, L.; Wei, W.B.; Jonas, J.B. Intraocular pressure and its normal range adjusted for ocular and systemic parameters. The Beijing Eye Study 2011. *PLOS ONE* **2018**, *13*, 1–16. https://doi.org/10.1371/journal.pone.0196926.
4. Haefliger, I.O.; von Arx, G.; Pimentel, A.R. Pathophysiology of intraocular pressure increase and glaucoma prevalence in thyroid eye disease: a mini-review. *Klin Monbl Augenheilkd* **2010**, *227*, 292–293.
5. Ghenciu, L.A.; Șișu, A.M.; Stoicescu, E.R.; Danila, A.I.; Iacob, R.; Sandesc, M.A.; Hațegan, O.A. Thyroid Eye Disease and Glaucoma: A Cross-Sectional Study Comparing Clinical Characteristics and Disease Severity. *Medicina (Kaunas)* **2024**, *60*, 1430. https://doi.org/10.3390/medicina60091430.
6. Rocks, M.C.; Bhatnagar, P.; Verticchio Vercellin, A.; Sala, L.; Siesky, B.; Antman, G.; Wood, K.; Sacco, R.; Harris, A. Mathematical Modeling and Artificial Intelligence to Explore Connections Between Glaucoma and the Gut Microbiome. *Medicina* **2025**, *61*. https://doi.org/10.3390/medicina61020343.
7. Li, J.; Huang, J.; Xu, S.; Zhang, S. Data-driven computational methods in ophthalmology: A multimodal perspective. *Eye Discovery* **2026**, *2*, 100026. https://doi.org/https://doi.org/10.1016/j.edisc.2026.100026.
8. Sacco, R.; Guidoboni, G.; Mauri, A.G. *A Comprehensive Physically Based Approach to Modeling in Bioengineering and Life Sciences*; Elsevier, Academic Press: Cambridge MA 02139, USA, 2019.
9. Kiel, J.W. Physiology of the intraocular pressure. In Proceedings of the Pathophysiology of the Eye: Glaucoma. Vol. 4; Feher, J., Ed., Budapest, 1998; pp. 109–144.
10. Kiel, J.W.; Hollingsworth, M.; Rao, R.; Chen, M.; Reitsamer, H.A. Ciliary blood flow and aqueous humor production. *Prog Retin Eye Res.* **2011**, *30*, 1–17.
11. Guidoboni, G.; Harris, A.; Cassani, S.; Arciero, J.; Siesky, B.; Amireskandari, A.; Tobe, L.; Egan, P.; Januleviciene, I.; Park, J. Intraocular Pressure, Blood Pressure, and Retinal Blood Flow Autoregulation: A Mathematical Model to Clarify Their Relationship and Clinical Relevance. *Investigative Ophthalmology & Visual Science* **2014**, *55*, 4105–4118, [https://arvojournals.org/arvo/content_public/journal/iovs/932991/i1552-5783-55-7-4105.pdf]. https://doi.org/10.1167/iovs.13-13611.
12. Sacco, R.; Chiaravalli, G.; Antman, G.; Guidoboni, G.; Verticchio, A.; Siesky, B.; Harris, A. The role of conventional and unconventional adaptive routes in lowering of intraocular pressure: Theoretical model and simulation. *Physics of Fluids* **2023**, *35*, 061902.
13. Friedland, A.B. A Hydrodynamic Model of Aqueous Flow in the Posterior Chamber of the Eye. *Bull. Math. Biol.* **1978**, *40*, 223–235.
14. Ferreira, J.A.; de Oliveira, P.; da Silva, P.M.; Murta, J.N. Numerical simulation of aqueous humor flow: From healthy to pathologic situations. *Applied Mathematics and Computation* **2014**, *226*, 777–792.
15. Dvoriashyna, M.; Foss, A.J.E.; Gaffney, E.A.; Repetto, R. A Mathematical Model of Aqueous Humor Production and Composition. *Invest. Ophthalmol. Vis. Sci.* **2022**, *63*, 1–1.

 doi:10.20944/preprints202606.0250.v1




16. Karimi, A.; Khan, S.; Razaghi, R.; Aga, M.; Rahmati, S.M.; White, E.; Kelley, M.J.; Jian, Y.; Acott, T.S. Segmental biomechanics of the normal and glaucomatous human aqueous outflow pathway. *Acta Biomaterialia* **2024**, *173*, 148–166. https://doi.org/https://doi.org/10.1016/j.actbio.2023.11.003.
17. Whitaker, S. Flow in porous media I: A theoretical derivation of Darcy's law. *Transp Porous Med* **1986**, *1*, 3–25.
18. Janssen, S.F.; Gorgels, T.G.M.F.; Bossers, K.; ten Brink, J.B.; Essing, A.H.W.; Nagtegaal, M.; van der Spek, P.J.; Jansonius, N.M.; Bergen, A.A.B. Gene Expression and Functional Annotation of the Human Ciliary Body Epithelia. *PLOS ONE* **2012**, *7*, 1–23. https://doi.org/10.1371/journal.pone.0044973.
19. Fautsch, M.P.; Johnson, D.H.; the Second ARVO/Pfizer Research Institute Working Group. Aqueous Humor Outflow: What Do We Know? Where Will It Lead Us? *Investigative Ophthalmology & Visual Science* **2006**, *47*, 4181–4187. https://doi.org/10.1167/iovs.06-0830.
20. Starling, E.H. On the Absorption of Fluids from the Connective Tissue Spaces. *The Journal of Physiology* **1896**, *19*, 312–326, [https://physoc.onlinelibrary.wiley.com/doi/pdf/10.1113/jphysiol.1896.sp000596]. https://doi.org/https://doi.org/10.1113/jphysiol.1896.sp000596.
21. Michel, C.C.; Woodcock, T.E.; Curry, F.R.E. Understanding and extending the Starling principle. *Acta Anaesthesiologica Scandinavica* **2020**, *64*, 1032–1037, [https://onlinelibrary.wiley.com/doi/pdf/10.1111/aas.13603]. https://doi.org/https://doi.org/10.1111/aas.13603.
22. Sacco, R.; Chiaravalli, G.; Guidoboni, G.; Layton, A.; Antman, G.; Shalem, K.W.; Verticchio, A.; Siesky, B.; Harris, A. Reduced-Order Model for Cell Volume Homeostasis: Application to Aqueous Humor Production. *Math. Comput. Appl.* **2025**, *30*, 13.
23. Noske, W.; Stamm, C.C.; Hirsch, M. Tight Junctions of the Human Ciliary Epithelium: Regional Morphology and Implications on Transepithelial Resistance. *Experimental Eye Research* **1994**, *59*, 141–149. https://doi.org/https://doi.org/10.1006/exer.1994.1092.
24. Delamare, N.A. Ciliary Body and Ciliary Epithelium. *Adv Organ Biol.* **2005**, *1*, 127–148.
25. Ethier, C.R.; Kamm, R.D.; Palaszewski, B.A.; Johnson, M.C.; Richardson, T.M. Calculations of flow resistance in the juxtacanalicular meshwork. *Investigative Ophthalmology & Visual Science* **1986**, *27*, 1741–1750.
26. Brubaker, R.F. The effect of intraocular pressure on conventional outflow resistance in the enucleated human eye. *Investigative Ophthalmology & Visual Science* **1975**, *14*, 286–292, [https://arvojournals.org/arvo/content_public/journal/iovs/933062/286.pdf].
27. Schey, K.L.; Wang, Z.; L. Wenke, J.; Qi, Y. Aquaporins in the eye: Expression, function, and roles in ocular disease. *Biochimica et Biophysica Acta (BBA) - General Subjects* **2014**, *1840*, 1513–1523. Aquaporins, https://doi.org/https://doi.org/10.1016/j.bbagen.2013.10.037.
28. Hamann, S.; Herrera-Perez, J.J.; Zeuthen, T.; Alvarez-Leefmans, F.J. Cotransport of water by the Na+-K+-2Cl- cotransporter NKCC1 in mammalian epithelial cells. *The Journal of Physiology* **2010**, *588*, 4089–4101, [https://physoc.onlinelibrary.wiley.com/doi/pdf/10.1113/jphysiol.2010.194738]. https://doi.org/https://doi.org/10.1113/jphysiol.2010.194738.
29. Shahidullah, M.; Al-Malki, W.H.; Delamere, N.A. Mechanism of Aqueous Humor Secretion, Its Regulation and Relevance to Glaucoma. In *Glaucoma*; Rumelt, S., Ed.; IntechOpen: Rijeka, 2011; chapter 1. https://doi.org/10.5772/26559.
30. Ibata, K.; Takimoto, S.; Morisaku, T.; Miyawaki, A.; Yasui, M. Analysis of Aquaporin-Mediated Diffusional Water Permeability by Coherent Anti-Stokes Raman Scattering Microscopy. *Biophysical Journal* **2011**, *101*, 2277–2283.
31. Ortega, J.M.; Rheinboldt, W.C. *Iterative Solution of Nonlinear Equations in Several Variables*; Vol. 30, *SIAM Classics in Applied Mathematics*, Society for Industrial and Applied Mathematics, 1970.
32. Emi, K.; Pederson, J.E.; Toris, C.B. Hydrostatic pressure of the suprachoroidal space. *Investigative ophthalmology & visual science* **1989**, *30*, 233–238.
33. Civan, M.M.; Peterson-Yantorno, K.; Sánchez-Torres, J.; Coca-Prados, M. Potential contribution of epithelial Na+ channel to net secretion of aqueous humor. *Journal of Experimental Zoology* **1997**, *279*, 498–503.
34. MATLAB. *version 9.10.0.1602886 (R2021a)*; The MathWorks Inc.: Natick, Massachusetts, 2021.
35. Brubaker, R.F. Goldmann's equation and clinical measures of aqueous dynamics. *Experimental Eye Research* **2004**, *78*, 633–637. Special issue in honour of David Maurice, https://doi.org/https://doi.org/10.1016/j.exer.2003.07.002.
36. Bikuna-Izagirre, M.; Aldazabal, J.; Extramiana, L.; Moreno-Montañés, J.; Carnero, E.; Paredes, J. Technological advances in ocular trabecular meshwork in vitro models for glaucoma research. *Biotechnology and Bioengineering* **2022**, *119*, 2698–2714, [https://analyticalsciencejournals.onlinelibrary.wiley.com/doi/pdf/10.1002/bit.28182]. https://doi.org/https://doi.org/10.1002/bit.28182.

 doi:10.20944/preprints202606.0250.v1




37. Wan, Y.; Guo, X.; Wang, N. Trabecular meshwork: A pivotal target for evolving glaucoma treatments. *Survey of Ophthalmology* **2025**, *70*, 1043–1060. https://doi.org/https://doi.org/10.1016/j.survophthal.2025.07.001.
38. Liu, Z.; Zheng, Y.; Zhao, J. Epigenetics of glaucoma in the trabecular meshwork. *Clin Epigenet* **2026**, *18*, 16. https://doi.org/https://doi.org/10.1186/s13148-025-02039-z.
39. Moledina, M.; Damato, E.M.; Lee, V. The changing landscape of thyroid eye disease: current clinical advances and future outlook. *Eye* **2024**, *38*, 1425–1437.
40. Costagliola, C.; dell'Omo, R.; Agnifili, L.; Bartollino, S.; Fea, A.M.; Uva, M.G.; Zeppa, L.; Mastropasqua, L. How many aqueous humor outflow pathways are there? *Surv Ophthalmol.* **2020**, *65*, 144–170.
41. Freddo, T.F.; Civan, M.; Gong, H., Aqueous Humor and the Dynamics of Its Flow: Mechanisms and Routes of Aqueous Humor Drainage. In *Albert and Jakobiec's Principles and Practice of Ophthalmology*; Albert, D.M.; Miller, J.W.; Azar, D.T.; Young, L.H., Eds.; Springer International Publishing: Cham, 2022; pp. 1989–2033. https://doi.org/10.1007/978-3-030-42634-7_163.
42. Tasneem, A.F.; Shwetha, B.A.; Mamata, N. Comparative study of serum and aqueous humour electrolyte levels in cataract patients. *International Journal of Recent Trends in Science and Technology* **2019**, *9*, 41–47.